Journal of Materials Chemistry A

Accepted Manuscript

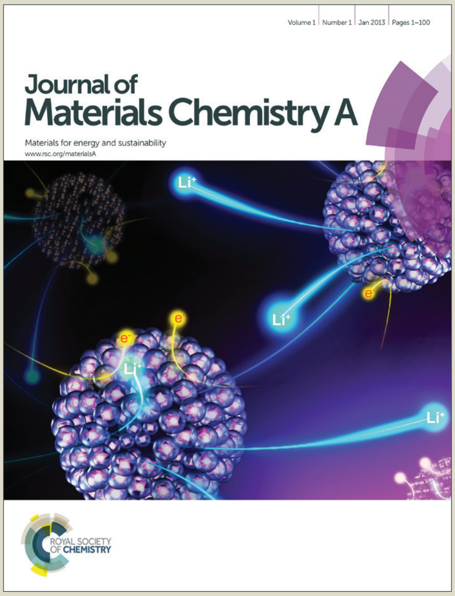

ROYAL SOCIETY OF CHEMISTRY

www.rsc.org/materialsA

$ZnFe_2O_4$@C/graphene nanocomposite as excellent anode materials for lithium batteries

Li Lin, Qinmin Pan*

(State Key Laboratory of Robotics and Systems, School of Chemical Engineering and Technology, Harbin Institute of Technology, Harbin 150001, *P*. *R*. China)

Corresponding author:

Qinmin Pan

Harbin Institute of Technology, Harbin 150001, *P*. *R*. China

E-mail: panqm@hit.edu.cn

Abstract

$ZnFe_2O_4$ is promising anode material for lithium ion batteries (LIBs) because of high theoretical capacity (1000.5 mAh g^{-1}), but its practical application is impeded by fast capacity fading and poor rate capability. To overcome these limitations, herein, core-shell structured $ZnFe_2O_4$@C nanoparticles were homogeneously anchored on the surface of graphene (G) nanosheets through a mussel-inspired process and followed by calcinations. The resulting $ZnFe_2O_4$@C/G nanocomposite delivered a reversible capacity of 705 mAh g^{-1} at 0.25 C after 180 cycles (with capacity retention of 99.4%), and high rate capability of 403.5 mAh g^{-1} at 5 C, exhibiting one of the best lithium storage properties among the reported $ZnFe_2O_4$ anodes. The excellent electrochemical performance is mainly related to the conducting, buffering and protective effects of carbon shells and graphene nanosheets on $ZnFe_2O_4$ nanoparticles. Considering its simplicity and effectiveness, the strategy might be extended to other anode materials with intrinsically low electronic conductivity, large volume-variation and severe agglomeration in the process of lithiation-delithiation.

Keywords: $ZnFe_2O_4$@C/graphene nanocomposite, core-shell nanostructure, graphene nanosheets, mussel-inspired process, lithium storage performances

Introduction

There is growing interest in designing and fabricating novel anode materials for lithium ion batteries (LIBs) with high energy density, long life and excellent rate capability.[1-3] Over the past few years, $ZnFe_2O_4$ has attracted much attention because of high theoretical capacity (1000.5 mAh g^{-1}).[4-13] Nevertheless, its practical application is still impeded by fast capacity fading and poor rate capability resulting from intrinsically low electronic conductivity, severe agglomeration and large volume-change in the process of lithiation-delithiation. To overcome these limitations, the common methods are introducing conductive agents and constructing nanostructures.[9,14-16] Among these strategies, coating $ZnFe_2O_4$ nanoparticles with a carbon layer greatly enhanced their lithium storage performance due to the conducting and buffering effects of carbon phase.[5,11] However, this approach did not lead to long-term cycling stability and high power density because of the inevitable agglomeration of paramagnetic $ZnFe_2O_4$ nanoparticles. A challenge remains in improving both long-term cycling life and high rate capability of $ZnFe_2O_4$ anode materials.

Recently, a double protection strategy, in which active nanoparticles are protected by both carbon shells and graphene nanosheets, effectively improves the cycling performance, especially rate capability of anode materials with low conductivity and large volume-change.[17-23] This strategy increases electrical contact and buffers the volume-change of active nanoparticles, as well as impedes their severe agglomeration to some extent.[17-23] The key of the strategy is to completely and homogeneously wrap each active nanoparticle with carbon shells (or graphene nanosheets), as well as anchor the wrapped nanoparticles onto graphene nanosheets. However, such a strategy is difficult to be applied for $ZnFe_2O_4$ because of severe agglomeration caused by paramagnetic properties.[24] From the standpoint of material design, a solution to the difficulty is to use carbon source that has high affinity (or strong adhesion) to each $ZnFe_2O_4$ nanoparticle and graphene (or graphite oxide) nanosheets.

In this regard, marine mussels might provide us an inspiration to achieve the above-mentioned goals because they exhibit high affinity (or strong adhesion) to a wide range of organic and inorganic substances. The strong adhesion of mussels is mainly associated with adhesive proteins containing high levels of catecholic ananlogues.[25,26] Inspired by this finding, catecholic derivatives like dopamine or polydopamine (PDA) were widely employed to construct a robust, continuous and homogenous layer on solids of various nature and morphologies.[27-30] In particular, the pyrolysis of polydopamine produces carbonaceous material containing N element that is beneficial for electronic conductivity.[31,32] All these features motivate us to propose a double protection strategy for $ZnFe_2O_4$ anode material through a mussel-inspired process.

Herein, core-shell structured $ZnFe_2O_4$@C nanoparticles are homogeneously anchored on the surface of graphene (G) nanosheets through a mussel-inspired process and subsequent calcinations (Scheme 1). To obtain such a $ZnFe_2O_4$@C/G nanocomposite, we use catecholic moieties that has high affinity to both $ZnFe_2O_4$ and graphite oxide as carbon source for the first time. The resulting $ZnFe_2O_4$@C/G nanocomposite show high reversible capacity, outstanding capacity retention, and excellent rate capability. Considering its simplicity and effectiveness, the strategy might be extended to other electrode materials with low electronic conductivity and large volume-change.

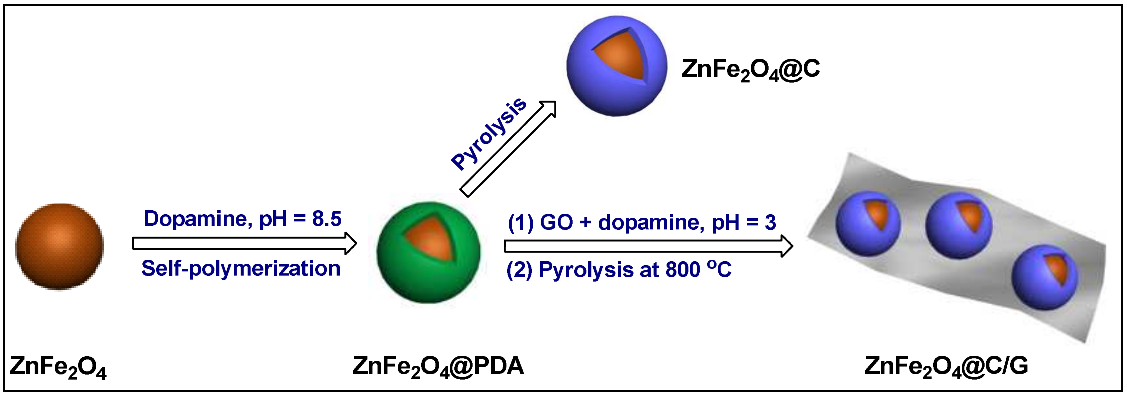

Scheme 1. Illustration for the fabrication of $ZnFe_2O_4$@C/G nanocomposite.

Experimental

(1) Materials and chemicals

Zinc chloride ($ZnCl_2$), ferric chloride hexahydrate ($FeCl_3 \cdot 6H_2O$) and Sodium acetate trihydrate ($NaAc \cdot 3H_2O$) were provided by Tianjin Bodi Chemical Co., Ltd. (China). Ethylene glycol ($HOCH_2CH_2OH$, EG) and polyethylene glycol ($HO(CH_2CH_2O)_nH$, PEG) were purchased from Institute of Tianjin Guangfu Fine Chemicals (China). Tris(hydroxymethyl) aminomethane hydrochloride (Tris-HCl) and dopamine hydrochloride were supplied by BASF Chemicals, Tianjin Co., Ltd. (China). Graphite powder was provided by Dongguan Tianrun Electronic Materials Co., Ltd. (China).

(2) Synthesis of $ZnFe_2O_4$ nanoparticles

$ZnFe_2O_4$ nanoparticles were synthesized according to a previous report.[33] Briefly, 2 mmol of $ZnCl_2$ and 4 mmol of $FeCl_3 \cdot 6H_2O$ were dissolved in 32 mL of ethylene glycol (EG). Then 2.88 g of sodium acetate (NaAc) and 0.8 g of polyethylene glycol (PEG) were added to the above solution. The resulting brick-red solution was maintained at 200 ^{o}C in a teflon-lined stainless-steel autoclave for 18 h. After it was cooled to room temperature, black $ZnFe_2O_4$ powder was collected by a magnet and subsequently washed with deionized water and ethanol three times, respectively.

(3) Synthesis of core-shell $ZnFe_2O_4$ @C nanoparticles and $ZnFe_2O_4$ @C/G nanocomposite

600 mg of $ZnFe_2O_4$ nanoparticles were dispersed in 300 mL of tris(hydroxymethyl) aminomethane hydrochloride solution (Tris-HCl, 10 mM, pH 8.5) by ultrasonication (300 W) for 30 min. Then 600 mg of dopamine was added to the resulting dispersion. After stirring for 12 h, $ZnFe_2O_4$ nanoparticles coated with polydopamine (*i.e.*, core-shell $ZnFe_2O_4$@PDA nanoparticles) were collected by a magnet and subsequently washed with deionized water three times.

Graphite oxide (GO) dispersion was synthesized through a modified Hummers method.[34] 20 mL of GO dispersion (2 mg mL^{-1}) was mixed with 120 mg of core-shell $ZnFe_2O_4$@PDA nanoparticles by ultrasonication (300 W) for 10 min. Then 80 mg of dopamine was added to the above mixture at pH 3.[29] After stirring for 18 h, $ZnFe_2O_4$@PDA/GO nanocomposite was collected by a magnet and then washed with deionized water three times.

The obtained $ZnFe_2O_4$@PDA and $ZnFe_2O_4$@PDA/GO powder were sintered at 400 ^{o}C for 2 h and then at 800 ^{o}C for another 2 h in argon atmosphere. After cooling to room temperature, core-shell $ZnFe_2O_4$@C nanoparticles and $ZnFe_2O_4$@C/G nanocomposite were obtained.

(4) Electrochemical measurements

$ZnFe_2O_4$@C/G (or core-shell $ZnFe_2O_4$@C) powder, polyvinylidene fluoride (PVDF) and carbon black (with a mass ratio of 8:1:1) were mixed in *N*-methyl-2-pyrrolidinone (NMP) to form a homogenous slurry. The slurry was pasted onto a copper foil and then dried at 100 ^{o}C in vacuum for 12 h. The resulting copper foil was punched to circle plates of 1.4 cm in diameter. Coin cells were assembled in a glove-box by using the plates, lithium foils and polypropylene separators. The electrolyte used was 1.0 M $LiPF_6$ in ethylene carbonate/diethyl carbonate/dimethyl carbonate (EC/DEC/DMC). The coin cells were tested by galvanostatic discharging-charging measurements on a battery tester (Neware BTS-53) at 0.01-3.0 V *vs*. Li/Li^{+}. Cyclic voltammetry (CV) was performed on a CHI 650D potentiostat between 0-3.0 V at a scan rate of 0.3 mV s^{-1}. Electrochemical impedance spectroscopy (EIS) was recorded on the potentiostat in the frequency range of 100 kHz-0.01 Hz with an AC voltage of 5 mV amplitude.

(5) Characterizations

Transmission electron microscopy (TEM) was conducted on a Hitachi H-7650. X-ray diffraction (XRD) patterns were recorded on a Rigaku-D/max rB. Raman spectroscopy was performed on a LabRAM XploRA with incident power of 1 mW and pumping wavelength of 532 nm. Thermogravimetric analysis (TGA) was measured by a Shimadzu STA-449F3 in air at a heating rate of 10 ^{o}C min^{-1}.

Results and discussion

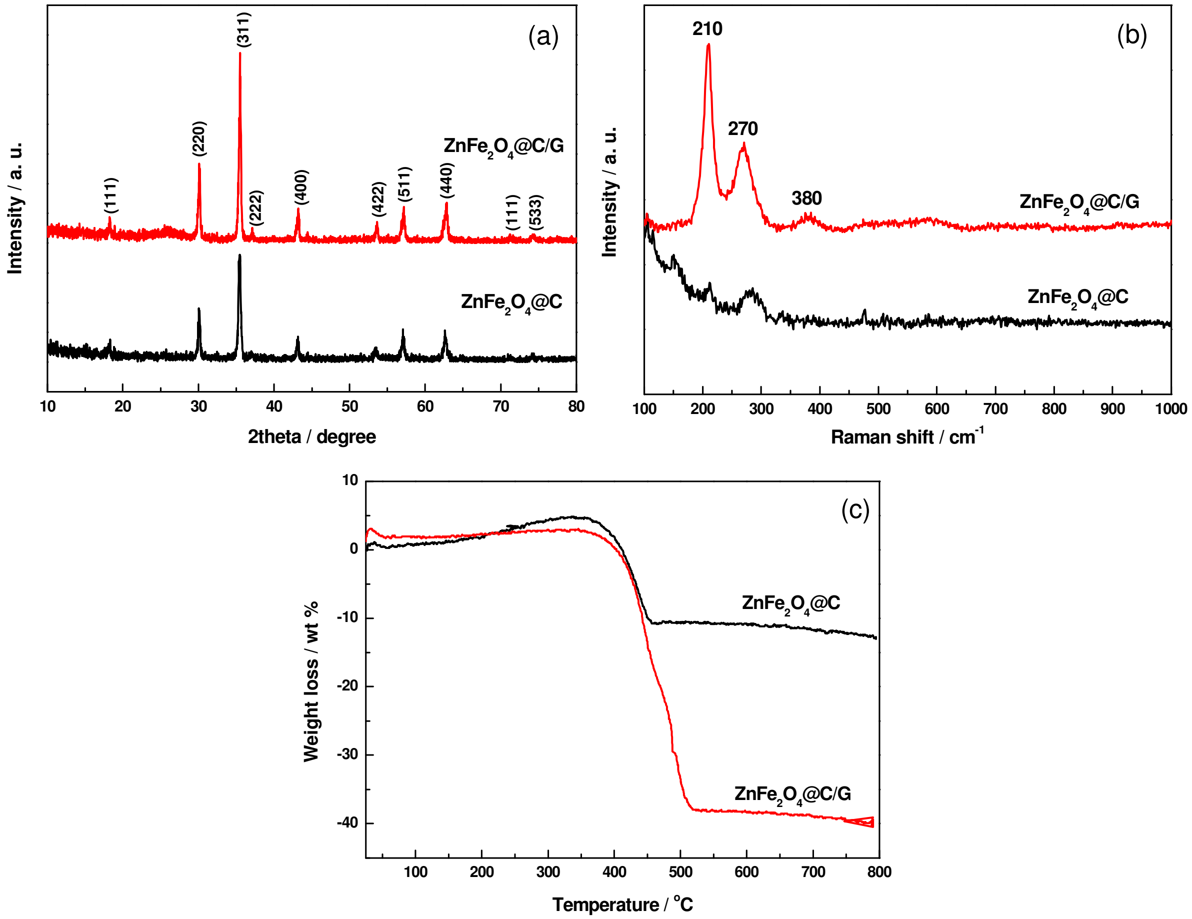

Fig. 1. XRD patterns (a), Raman spectra (b) and TGA curves (c) of core-shell $ZnFe_2O_4$@C nanoparticles and $ZnFe_2O_4$@C/G nanocomposite.

To synthesize $ZnFe_2O_4$@C/G nanocomposite, $ZnFe_2O_4$ nanoparticles were firstly wrapped with a homogeneous layer of polydopamine (PDA) to form core-shell nanostructure.[30] Then the resulting core-shell $ZnFe_2O_4$@PDA nanoparticles were immobilized onto graphite oxide (GO) nanosheets in the presence of dopamine at pH 3.[29] After calcinations at 800 °C, core-shell $ZnFe_2O_4$@C nanoparticles were anchored on the surface of graphene nanosheets to form $ZnFe_2O_4$@C/G nanocomposite (Scheme 1). At first, the chemical compositions of the obtained $ZnFe_2O_4$@C and $ZnFe_2O_4$@C/G nanocomposites were identified by XRD, Raman and TGA measurements. Fig. 1a shows the XRD patterns of $ZnFe_2O_4$@C and $ZnFe_2O_4$@C/G nanocomposites. All the diffraction peaks in Fig.

1a are well consistent with cubic $ZnFe_2O_4$ (Fig. S1a, ESI). No distinct peaks ascribed to carbon are found in the XRD pattern of $ZnFe_2O_4$@C, suggesting amorphous nature of the carbon phase. The feature peaks of GO are observed in XRD pattern (Fig. S1b, ESI) and Raman spectra (Fig. S2b, ESI). And the feature XRD peaks of GO are no longer observed for $ZnFe_2O_4$@C/G nanocomposite, indicating that GO was completely reduced to graphene after calcinations. In contrast, a broad peak assigned to the stacking of graphene layers appears at around 26°. Raman spectroscopy was further used to investigate the crystalline structure of $ZnFe_2O_4$ and carbonaceous phases. Fig. 1b is the Raman spectra of core-shell $ZnFe_2O_4$@C nanoparticles and $ZnFe_2O_4$@C/G nanocomposite. These nanomaterials show feature bands of $ZnFe_2O_4$ in the frequency range of 100-1000 cm^{-1} (Fig. S2a, ESI).[12] TGA was employed to determine carbon content in $ZnFe_2O_4$@C and $ZnFe_2O_4$@C/G nanocomposites (Fig. 1c). The results show that there are 14.4 and 38.4 wt% of carbon presented in $ZnFe_2O_4$@C and $ZnFe_2O_4$@C/G nanocomposites, respectively. Additionally, EDX plots and XPS results reveal that the carbon phase in the nanocomposites contains N element that is beneficial for electrical conductivity (Fig. S3 and S4, ESI).

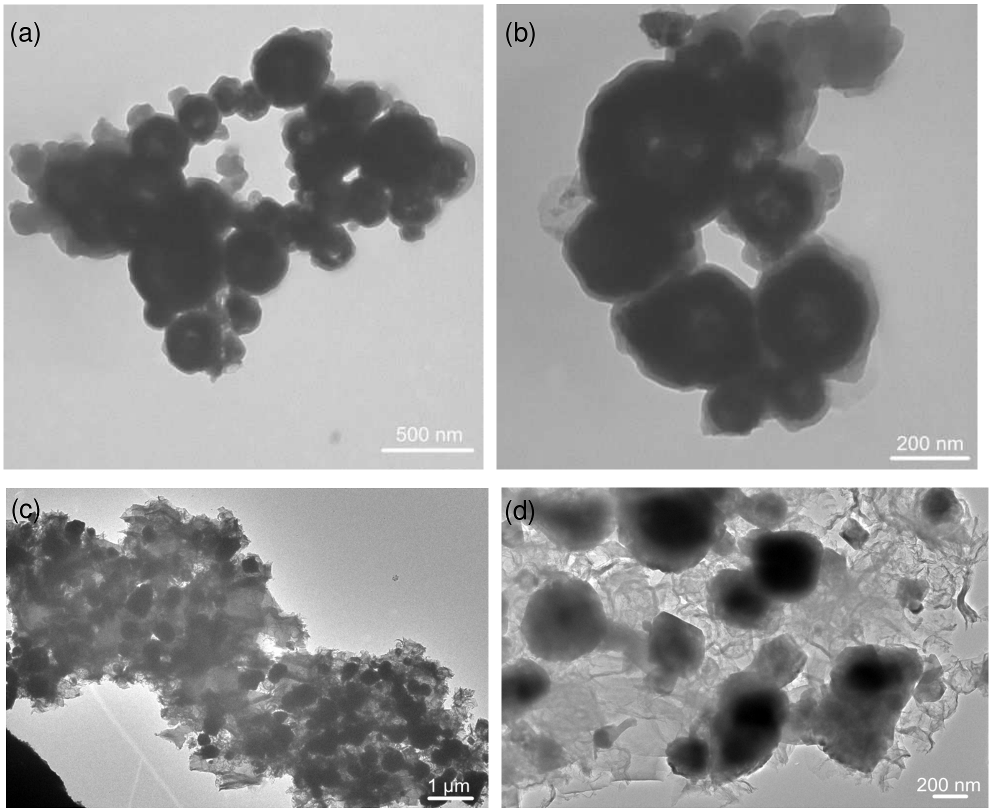

Fig. 2. TEM images of (a, b) core-shell $ZnFe_2O_4$@C nanoparticles and (c, d) $ZnFe_2O_4$@C/G nanocomposites.

The microstructure of core-shell $ZnFe_2O_4$@C nanoparticles and $ZnFe_2O_4$@C/G nanocomposites was further investigated by TEM observations (Fig. 2). For comparison, we also recorded the TEM images of the pristine $ZnFe_2O_4$, core-shell $ZnFe_2O_4$@PDA nanoparticles (Fig. S5, ESI), and the size distribution of $ZnFe_2O_4$ nanoparticles (Fig. S6, ESI). Compared with its $ZnFe_2O_4$@PDA precursor, $ZnFe_2O_4$@C nanocomposite remains the core-shell nanostructure because each $ZnFe_2O_4$ nanoparticle is wrapped by a homogenous and continuous carbon shell of ~20 nm in thickness (Fig. 2a-b). The continuity and homogeneity of these carbon shells indicate that polydopamine layer has high affinity to $ZnFe_2O_4$ nanoparticles and thus effectively preventing their severe agglomeration caused by paramagnetism.[24] The high affinity of polydopamine is associated with its catecholic group that can coordinate with Fe^{3+} of $ZnFe_2O_4$.[27,28] For $ZnFe_2O_4$@C/G nanocomposite (Fig. 2c-d), $ZnFe_2O_4$@C nanopaticles homogenously cover on the surface of graphene sheets, suggesting that carbon shells together with graphene sheets construct hybrid conducting and buffering matrix for $ZnFe_2O_4$ nanoparticles. The above results demonstrate the possibility to fabricate $ZnFe_2O_4$@C/G nanocomposite by combining calcinations and the high affinity of catecholic derivatives.

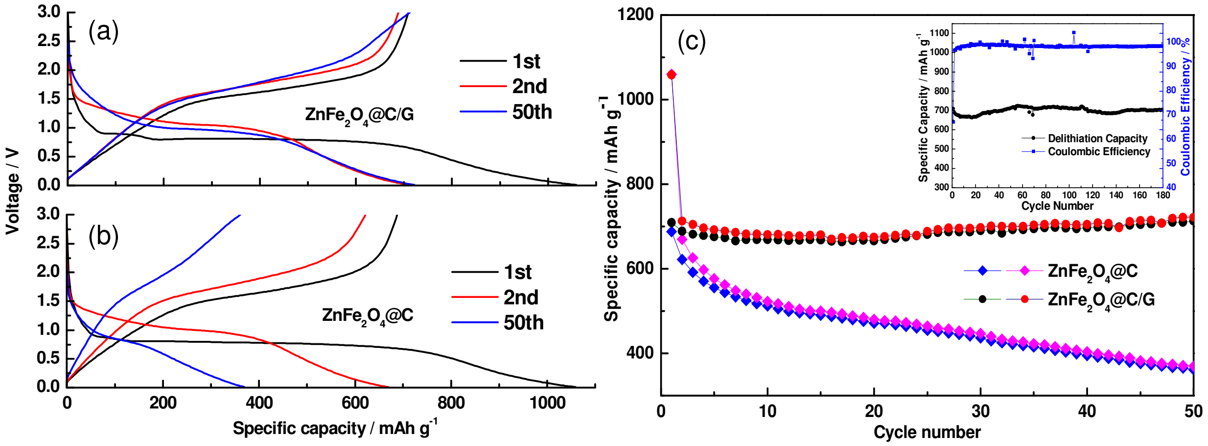

Fig. 3. Voltage profiles (a, b) and cycling performance (c) of the $ZnFe_2O_4$@C and $ZnFe_2O_4$@C/G electrodes at a current density of 232 mA g^{-1}. Inset of Fig. 3c is the cycling performance of the $ZnFe_2O_4$@C/G electrode.

Then the lithium storage performance of the resulting $ZnFe_2O_4$@C and $ZnFe_2O_4$@C/G nanocomposites was investigated by galvanostatic discharging-charging and cyclic voltammetry measurements. Fig. 3a is the voltage profiles of a typical $ZnFe_2O_4$@C/G electrode at a current density of 232 mA g^{-1} (~0.25 C). In the initial lithiation process, there are two voltage plateaus located at 0.90 and 0.81 V, respectively. These plateaus are replaced by a long slope in the subsequent lithiation processes. Notably, dramatic voltage drop from open circuit voltage (OCV) to 1.1 V takes place in the initial lithiation process, which is associated with the phase transition from $ZnFe_2O_4$ to $Li_xZnFe_2O_4$ (x~0.5).[7,10] In contrast, only a voltage plateau is observed at 1.5-2.2 V in the delithiation processes. The voltage profiles of the $ZnFe_2O_4$@C/G electrode are consistent with its CV results (Fig. S7, ESI). The electrode delivers an initial lithiation and delithiation capacity of 1058.5 and 709.3 mAh g^{-1}, respectively, corresponding to a coulombic efficiency of 67.0%. The low coulombic efficiency is mainly related to the decomposition of electrolyte and subsequent formation of solid electrolyte interface (SEI) film.[3-8] Under the same conditions, the $ZnFe_2O_4$@C electrode exhibits an initial lithiation and delithiation capacity of 1059.5 and 687.9 mAh g^{-1}, respectively (Fig. 3b). The capacities and coulombic efficiency (64.9%) are much closed to those of the $ZnFe_2O_4$@C/G electrode. However, the $ZnFe_2O_4$@C/G electrode shows a much better cycling characteristic than its $ZnFe_2O_4$@C counterpart. Fig. 3c is the cycling performance of the two electrodes at a current density of 232 mA g^{-1}. The capacity of the $ZnFe_2O_4$@C/G electrode slowly decreases to 663.6 mAh g^{-1} in the initial 17 cycles, but it slightly increases to 712.5 mAh g^{-1} at the 50th cycle. The slight increase in capacity with cycling number is mainly attributed to the reversible formation of a polymeric gel-like SEI film through electrolyte decomposition.[6,9,13] After discharging-charging for 180 cycles, the electrode exhibits a delithiation capacity of 705 mAh g^{-1}, about 99.4% of the initial value. To our knowledge, this is one of the best results for long-term cycling performance of $ZnFe_2O_4$ anodes.[4-13] In contrast, the $ZnFe_2O_4$@C electrode continuously decreases its delithiation capacity from 687.9 to 361.1 mAh g^{-1} after discharging-charging for 50 cycles, implying that carbon shells cannot ensure stable cycling performance. The rapid capacity fading is mainly due to intrinsically low electronic conductivity and large volume change of $ZnFe_2O_4$ nanoparticles in the lithiation-delithiation process, which results in the electrical isolation of active material.[4-13] These results indicate the important role of graphene nanosheets in the cycling characteristic of the $ZnFe_2O_4$-based anodes.

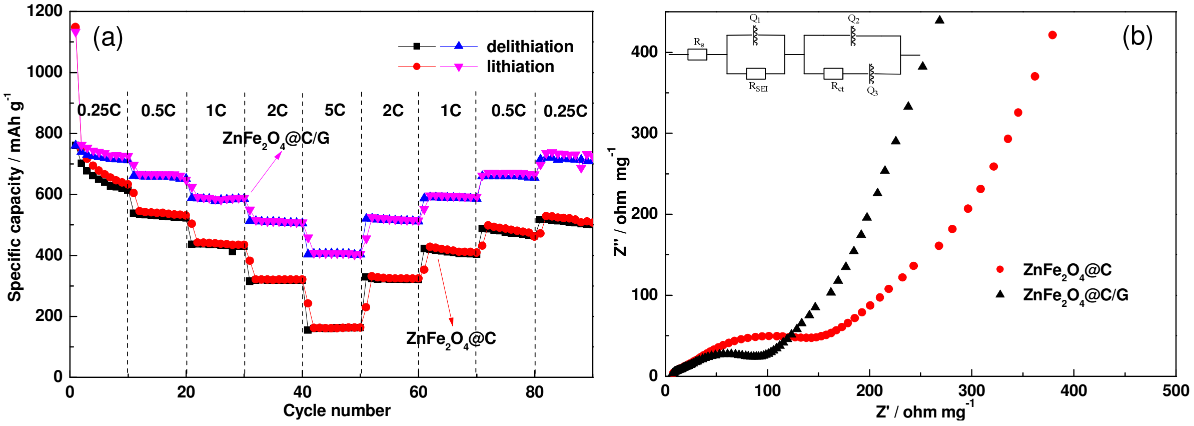

Fig. 4. Rate capability (a) and electrochemical impedance spectra (b) of the $ZnFe_2O_4$@C and $ZnFe_2O_4$@C/G electrodes. The EIS were recorded at the end of the 20th cycle. Inset is the equivalent circuit used in this study. 1C = 928 mA g^{-1}.

The rate capability of the $ZnFe_2O_4$@C/G and $ZnFe_2O_4$@C electrodes was further examined at different current densities (Fig. 4a). The $ZnFe_2O_4$@C/G electrode exhibits higher reversible capacities than its $ZnFe_2O_4$@C counterpart, and the difference is enlarged as current density is increased from 0.25 to 5 C. At the rates of 0.25 C, 0.5 C, 1 C and 2 C, the $ZnFe_2O_4$@C/G electrode delivers delithiation capacities of 711.9 (10th), 650.9 (20th), 584.9 (30th) and 505.4 mAh g^{-1} (40th), respectively. Under the same current densities, the $ZnFe_2O_4$@C electrode only exhibits delithiation capacities of 613.3 (10th), 522.2 (20th), 430.2 (30th), 319 mAh g^{-1} (40th), respectively. Even at a high rate of 5 C, the $ZnFe_2O_4$@C/G electrode is able to keep a capacity of 403.5 mAh g^{-1}, still greater than that of the $ZnFe_2O_4$@C (163.6 mAh g^{-1}). After current density is stepwise reduced to 0.25 C, the $ZnFe_2O_4$@C/G electrode recovers its capacity to 708.1 mAh g^{-1} at the 90th cycle, while that of the $ZnFe_2O_4$@C electrode is only 499.8 mAh g^{-1}. We also compared the present results with those of the previous studies,[4-13,35] which reveals that the $ZnFe_2O_4$@C/G electrode exhibits one of the best lithium storage performances, especially in rate capability and cycling characteristic. For example, the electrode shows much better cycling performance than its $ZnFe_2O_4$ counterparts like $ZnFe_2O_4$ nanofibers,[4] $ZnFe_2O_4$/C hollow spheres,[6] $ZnFe_2O_4$/graphene hybrid,[35] and so on.[9,10,13] But it does not deliver a reversible capacity as high as carbon coated $ZnFe_2O_4$ nanoparticles,[5] hollow spherical $ZnFe_2O_4$,[7] and MWCNT-$ZnFe_2O_4$ nanocomposite.[8] To our knowledge, rare studies reported hybrid carbon/graphene matrix for $ZnFe_2O_4$ through a facile bio-inspired process with an aim for improving lithium storage performance.

Table 1. Fitting results of the EIS spectra recorded for the $ZnFe_2O_4$@C and $ZnFe_2O_4$@C/G electrodes.

Electrodes	**R_s / Ω mg^{-1}**	**R_{SEI} / Ω mg^{-1}**	**R_{ct} / Ω mg^{-1}**
$ZnFe_2O_4$@C	4.1	132.2	145.9
$ZnFe_2O_4$@C/G	4.5	84.6	81.1

The better electrochemical performance of the $ZnFe_2O_4$@C/G electrode was also supported by electrochemical impedance spectroscopy (EIS) measurements. Fig. 4b is the Nyquist plots of the $ZnFe_2O_4$@C and $ZnFe_2O_4$@C/G electrodes recorded at the end of the 20th cycle. Each plot consists of a semicircle at high-medium frequency range and a declined line at low frequency region. The $ZnFe_2O_4$@C/G electrode exhibits a smaller semicircle than its $ZnFe_2O_4$@C counterpart, indicating a lower inner resistance of the former. Indeed, the fitting results in Table 1 reveal that the former displays a lower charge transfer resistance (R_{ct}, 81.1 Ω mg^{-1}) than the $ZnFe_2O_4$@C electrode (145.9 Ω mg^{-1}). The lower R_{ct} is beneficial for improving the cycling performance and rate capability of the $ZnFe_2O_4$@C/G electrodes.[17]

The excellent cycling performance and rate capability of the $ZnFe_2O_4$@C/G electrode are due to the following reasons. At first, uniform and continuous carbon shells protect $ZnFe_2O_4$ nanoparticles from direct contact with electrolyte, contributing to the structural integrity of the nanoparticles in the lithiaiton-delithiation process. Additionally, these carbon shells not only buffer the volume expansion of $ZnFe_2O_4$ nanoparticles but also keep stable electronic conductivity in the process of lithiation-delithiation.[5,6,11,18-23] Secondly, graphene nanosheets impede the agglomeration of $ZnFe_2O_4$@C nanoparticles to some extent, as well as increase the contact area between the nanoparticles and electrolyte. More importantly, flexible graphene nanosheets also improve the electrical contact and accommodate the volume changes of the active materials, forming another buffering and conductive network for core-shell $ZnFe_2O_4$@C nanoparticles. Therefore, the excellent lithium storage performance of the $ZnFe_2O_4$@C/G electrode mainly results from the conducting, buffering and protective effects of hybrid carbon/graphene matrix on $ZnFe_2O_4$ nanoparticles.

Conclusions

In summary, core-shell $ZnFe_2O_4@C$ nanoparticles were anchored onto graphene nanosheets through a mussel-inspired process and subsequent calcinations for the first time. The resulting $ZnFe_2O_4@C/G$ nanocomposite exhibited a reversible capacity of 705 mAh g^{-1} at 0.25 C after 180 cycles (with capacity retention of 99.4%), and a rate capability of 403.5 mAh g^{-1} at 5 C. These results are not only much better than those of core-shell $ZnFe_2O_4@C$ nanoparticles but also one of the best performances among the existing $ZnFe_2O_4$ anode materials. The excellent electrochemical performance is believed to originate from the conductive, buffering and protective effects of hybrid carbon/graphene matrix on $ZnFe_2O_4$ nanoparticles. Because catecholic derivatives show high affinity to solids with various nature and morphologies, the strategy might be extended to other anode materials such as Si, SnO_2, Sn, and Ge, and so on.

Electronic Supplementary Information:

XRD patterns, Raman spectra of $ZnFe_2O_4$ nanoparticles and graphite oxide; EDX plots, cyclic voltommograms of core-shell $ZnFe_2O_4@C$ nanoparticles and $ZnFe_2O_4@C/G$ nanocomposite; TEM images of $ZnFe_2O_4$ nanoparticles and core-shell $ZnFe_2O_4@PDA$ nanoparticles.

Acknowledgement

This study was financially supported by a self-planned task of the State Key Laboratory of Robotics and System of Harbin Institute of Technology (SKLRS200901C) and National Natural Science Foundation of China (51473041).

References

1. J. M. Tarascon and M. Armand, *Nature*, 2001, **414**, 359–367.
2. P. G. Bruce, B. Scrosati and J. M. Tarascon, *Angew. Chem. Int. Ed.*, 2008, **47**, 2930–2946.
3. P. Poizot, S. Laruelle, S. Grugeon, L. Dupont and J. M. Tarascon, *Nature*, 2000, **407**, 496–499.
4. P. F. Teh, Y. Sharma, S. S. Pramana and M. Srinivasan, *J. Mater. Chem.*, 2011, **21**, 14999–15008.
5. D. Bresser, E. Paillard, R. Kloepsch, S. Krueger, M. Fiedler, R. Schmitz, D. Baither, M. Winter and S. Passerini, *Adv. Energy Mater.*, 2012, **3**, 513–523.
6. Y. F. Deng, Q. M. Zhang, S. D. Tang, L. T. Zhang, S. N. Deng, Z. C. Shi and G. H. Chen, *Chem. Commun.*, 2011, **47**, 6828–6830.
7. X. W. Guo, X. Lu, X. P. Fang, Y. Mao, Z. X. Wang, L. Q. Chen, X. X. Xu, H. Yang and Y. N. Liu, *Eectrochem. Commun.*, 2010, **12**, 847–850.
8. J. H. Sui, C. Zhang, D. Hong, J. Li, Q. Cheng, Z. G. Li and W. Cai, *J. Mater. Chem.*, 2012, **22**, 13674–13681.
9. Y. N. NuLi, Y. Q. Chu, Q. Z. Qin, *J. Electrochem. Soc.*, 2004, **151**, A1077–A1083.
10. Y. Ding, Y. F. Yang and H. X. Shao, *Electrochim. Acta*, 2011, **56**, 9433–9438.
11. F. Mueller, D. Bresser, E. Paillard, M. Winter and S. Passerini, *J. Power Sources*, 2013, **236**, 87–94.
12. H. Xia, Y. Y. Qian, Y. S. Fu and X. Wang, *Solid State Sciences*, 2013, **17**, 67–71.
13. Y. Sharma, N. Sharma, G. V. Subba Rao and B. V. R. Chowdari, *Electrochim. Acta*, 2008, **53**, 2380–2385.
14. B. J. Li, H. Q. Cao, J. Shao, G. Q. Li, M. Z. Qu and G. Yin, *Inorg. Chem.*, 2011, **50**, 1628–1632.
15. J. F. Li, J. Z. Wang, X. Liang, Z. J. Zhang, H. K. Liu, Y. T. Qian and S. L. Xiong, *ACS Appl. Mater. Interfaces*, 2014, **6**, 24–30.
16. J. F. Li, J. Z. Wang, D. Wexler, D. Q. Shi, J. W. Liang, H. K. Liu, S. L. Xiong and Y. T. Qian, *J. Mater. Chem. A*, 2013, **1**, 15292–15299.
17. D. J. Xue, S. Xin, Y. Yan, K. C. Jiang, Y. X. Yin, Y. G. Guo and L. J. Wan, *J. Am. Chem. Soc.*, 2012, **134**, 2512–2515.
18. Y. Z. Su, S. Li, D. Q. Wu, F. Zhang, H. W. Liang, P. F. Gao, C. Cheng and X. L. Feng, *ACS Nano*, 2012, **6**, 8349–8356.
19. M. Zhou, T. W. Cai, F. Pu, H. Chen, Z. Wang, H. Y. Zhang and S. Y. Guan, *ACS Appl. Mater. Interfaces*, 2013, **5**, 3449–3455.

20. Y. M. Ren, J. Zhang, Y. Y. Liu, H. B. Li, H. J. Wei, B. J. Li and X. Y. Wang, *ACS Appl. Mater. Interfaces*, 2012, **4**, 4776–4780.
21. J. Zhu, D. N. Lei, G. H. Zhang, Q. H. Li, B. A. Lu and T. H. Wang, *Nanoscale*, 2013, **5**, 5499–5505.
22. B. Luo, B. Wang, X. L. Li, Y. Y. Jia, M. H. Liang and L. J. Zhi, *Adv. Mater.*, 2012, **24**, 3538–3543.
23. W. Wei, S. B. Yang, H. X. Zhou, I. Lieberwirth, X. L. Feng and K. Müllen, *Adv. Mater.*, 2013, **25**, 2909–2914.
24. M. Wang, Z. Ai, and L. Zhang, *J. Phys. Chem. C*, 2008, **112**, 13163–13170.
25. H. Lee, S. M. Dellatore, W. M. Miller and Messersmith, *Science*, 2007, **318**, 426–430.
26. H. G. Silverman and F. F. Roberto, *Mar. Biotechnol.*, 2007, **9**, 661–681.
27. Q. Ye, F. Zhou and W. M. Liu, *Chem. Soc. Rev.*, 2011, **40**, 4244–4258.
28. S. Josep, S. P. Javier, B. Felix and R. M. Daniel, *Adv. Mater.*, 2013, **25**, 653–701.
29. Q. Zhu and Q. M. Pan, *ACS Nano*, 2014, **8**, 1402–1409.
30. F. T. Liu, F. H. Sun and Q. M. Pan, *J. Mater. Chem. A*, 2014, **2**, 11365–11371.
31. R. Liu, S. M. Mahurin, C. Li, R. R. Unocic, J. C. Idrobo, H. J. Gao, S. J. Pennycook and S. Dai, *Angew. Chem. Int. Ed.*, 2011, **50**, 6799–6802.
32. C. Lei, F. Han, D. Li, W. C. Li, Q. Sun, X. Q. Zhang and A. H. Lu, *Nanoscale*, 2013, **5**, 1168–1175.
33. H. Deng, X. L. Li, Q. Peng, X. Wang, J. P. Chen and Y. D. Li, *Angew. Chem. Int. Ed.*, 2005, **44**, 2782–2785.
34. W. S. Hummers and R. E. Offeman, *J. Am. Chem. Soc.*, 1958, **80**, 1339.
35. W. T. Song, J. Xie, S. Y. Liu, G. S. Cao, T. J. Zhu and X. B. Zhao, *New J. Chem.*, 2012, **36**, 2236–2241.

TOC

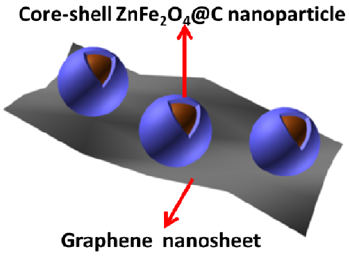

$ZnFe_2O_4$@C/G nanocomposite exhibiting excellent lithium storage performance was synthesized through a mussel-inspired process and subsequent calcinations.